Energy 58 (2013) 404–416

Contents lists available at SciVerse ScienceDirect

Energy

journal homepage: www.elsevier.com/locate/energy

Thermodynamic analysis of a dual loop heat recovery system with trilateral cycle applied to exhaust gases of internal combustion engine for propulsion of the 6800 TEU container ship

Byung Chul Choi [a,*], Young Min Kim [b]

[a] Environment & Plant Team, Korean Register of Shipping, Seoul, Republic of Korea
[b] Department of Engine Research, Korea Institute of Machinery & Materials, Daejeon, Republic of Korea

ARTICLE INFO

Article history:
Received 21 January 2013
Received in revised form
14 May 2013
Accepted 15 May 2013
Available online 28 June 2013

Keywords:
Trilateral cycle
Organic Rankine cycle
Dual loop
Marine diesel engine
Container ship
Energy efficiency

ABSTRACT

A dual loop waste heat recovery power generation system that comprises an upper trilateral cycle and a lower organic Rankine cycle, in which discharged exhaust gas heat is recovered and re-used for propulsion power, was theoretically applied to an internal combustion engine for propulsion in a 6800 TEU container ship. The thermodynamic properties of this exhaust gas heat recovery system, which vary depending on the boundary temperature between the upper and lower cycles, were also investigated. The results confirmed that this dual loop exhaust gas heat recovery power generation system exhibited a maximum net output of 2069.8 kW, and a maximum system efficiency of 10.93% according to the first law of thermodynamics and a maximum system exergy efficiency of 58.77% according to the second law of thermodynamics. In this case, the energy and exergy efficiencies of the dual loop system were larger than those of the single loop trilateral cycle. Further, in the upper trilateral cycle, the volumetric expansion ratio of the turbine could be considerably reduced to an adequate level to be employed in the practical system. When this dual loop exhaust gas heat recovery power generation system was applied to the main engine of the container ship, which was actually in operation, a 2.824% improvement in propulsion efficiency was confirmed in comparison to the case of a base engine. This improvement in propulsion efficiency resulted in about 6.06% reduction in the specific fuel oil consumption and specific CO_2 emissions of the main engine during actual operation.

1. Introduction

The development of eco-friendly ships has been attracting increasing interest because environmental pollution of the ocean has become increasingly serious owing to shipping, and because rising oil prices have meant that the international crude oil prices have exceeded USD100 per barrel. In particular, in order to curb fuel costs and CO_2 (carbon dioxide) emissions, future eco-friendly ships will require “green” ship technology that offers both high energy efficiency and eco-friendliness, through innovative use of eco-friend energy sources and improvement in existing devices.

The principle greenhouse gas generated in the field of shipping is carbon dioxide (CO_2), and the emission has a variety of sources, including engine exhaust gas, freight transport (packaging), and refrigerants. CO_2 is primarily emitted as an exhaust gas from ship components such as the main engine, auxiliary engine, and boiler. Total CO_2 emissions generated in the domestic and overseas shipping industries reached a record of about 1 billion tons in 2007, constituting 3.3% of global CO_2 emissions [1].

The MEPC (Marine Environment Protection Committee) of the IMO (International Maritime Organization) under the umbrella of the UN has modified its marine pollution prevention convention, i.e., the MARPOL Annex VI, in order to lower the CO_2 emitted from newly built ships and existing ships [2]. According to the modified convention, an EEDI (Energy Efficiency Design Index), which indexes CO_2 emissions properties relative to the type and size of a ship, will be introduced for ships involved in various applications that are contracted and newly built starting from January 2013, and the design of new ships will include constraints on the CO_2 emissions. In addition, an EEOI (Energy Efficiency Operational Indicator) was introduced for indexing CO_2 emitted per unit transport by ships currently in operation, in order to enable ship operators to voluntarily monitor and manage energy efficiency.

Although there have been various technological improvements to ship building and propulsion systems with regard to maximization of a ship’s energy efficiency, the amount of CO_2 emitted from

* Corresponding author. Tel.: +82 10 2819 4558.
E-mail address: byungchul.choi@gmail.com (B.C. Choi).

0360-5442/$ – see front matter © 2013 Elsevier Ltd. All rights reserved.
http://dx.doi.org/10.1016/j.energy.2013.05.017

a ship is directly related to the amount of fuel consumed by the internal combustion engine propelling the ship. Therefore, a power generation system that makes use of the waste heat from its main engine (a Waste Heat Recovery System) could be a principle technology that drastically reduces CO_2 emissions [3].

Waste heat recovery power generation systems that have been applied to a ship's main engine can be broadly classified into two types, i.e., a power turbine scheme, in which the kinetic energy of the gas is utilized to directly drive the turbines, and a steam turbine scheme [4], which applies a Rankine cycle using water as the working fluid; a combination of both these schemes could also be used [5]. In particular, because the steam turbine scheme uses as low-temperature exhaust gas, at about 550 K, as a heat source, superheated steam is produced for a multi-step heat exchange via a HP and LP (high pressure and low pressure) feed water heater; a mixed-pressure turbine has also been applied. This scheme has limited ability to maximize energy efficiency, because of exergy loss of the low-temperature exhaust-gas heat source during the process of boiling the water.

Various studies have applied a Rankine cycle using an organic working fluid with a lower boiling point than water, in order to recover the low-temperature heat source discarded from the engine. Further, some studies have compared the efficiency and output for primarily pure [6] or mixed working fluids [7] in order to select an optimal working fluid. There has also been research on combined heat recovery systems [8] that integrate devices for cooling water, exhaust gas [9], and intake air [10] as well as exhaust gas recirculation [11]. Recently, dual loop waste heat recovery power generation systems have been actively researched, in order to simultaneously recover heat from high-temperature exhaust gases and low-temperature cooling water discarded from engines [12], including the wasting heat of intake air [13]. Such research has mainly investigated the performance of such heat recovery systems under the waste heat conditions of a small- to medium-sized engine for vehicles or for power generation.

Recently, a notable study was conducted by Johann Fischer, which compared trilateral cycles in which saturated water was directly injected into the expander as a working fluid and organic Rankine cycles injected with pure organic working fluids [14]. It has been reported that the exergy efficiency of the trilateral cycle was larger than that of organic Rankine cycles. This is because the minimized exergy loss in the trilateral cycle, owing to the temperature difference between the heat source and the two-phase water system (liquid and steam) in the boiling process, with consideration of the pinch temperature. However, as the volume flow rate of water at the outlet of expander significantly increases with the phase transition from liquid to vapor, the two-phase expander is required to be unrealistically large with a positive displacement, which may hinder its application to the practical system.

In the present study, we investigated a heat recovery power generation system applied to exhaust gas discharged from the main engine of a container ship that was actually in operation. The main engine's fuel consumption rate, shaft output, and exhaust gas temperature and the ship's speed were measured on a full-scale ship and two representative sets of exhaust gas conditions were selected on the basis of this measured data. A dual loop waste heat recovery power generation system using water and R1234yf as the working fluid was theoretically applied to these two heat sources. The dual loop system consisting of an upper trilateral cycle and a lower organic Rankine cycle was adopted to overcome the limitations of the single loop trilateral cycle. We also investigated the thermodynamic properties of the waste heat recovery power generation system with regard to changes in the boundary temperature between the dual loops, and discuss the manner in which the recovered power enables conservation of main engine fuel and reduction in the CO_2 emissions.

2. The container ship

The ship selected for the present study was the Hyundai Jakarta, a 6800 TEU containership that was built on 12 December 2006. The ship has a gross tonnage of 74,651 tons, and is 288.4 m length, 40.0 m beam, and 24.2 m draught. The maximum output, i.e., MCR (Maximum Continuous Rating), of the internal combustion engine for propulsion (HYUNDAI-MAN B&W, 12K98 MC-C Mk6) is 68,520 kW at 104 rpm [15].

2.1. Data collection method

Fig. 1 is a schematic of an internal combustion engine for propulsion as well as a dual loop waste heat recovery power

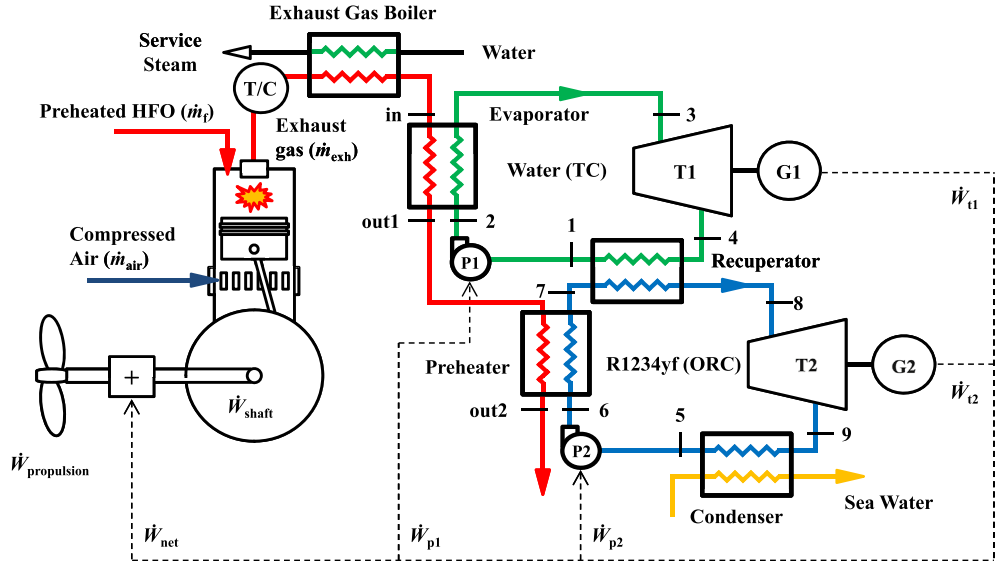

Fig. 1. Schematic of a dual loop heat recovery system applied to exhaust gas of an internal combustion engine for propulsion.

generation system applied to the exhaust gases of the engine. The main engine is a 2-stroke engine; air $\dot{m}_{air}$ compressed by a turbocharger using kinetic energy from the exhaust gas is fed to the inside of a combustion chamber, and is combusted together with injected HFO fuel $\dot{m}_f$. Here, $\dot{W}_{shaft}$ is a shaft for the combustion gas, which expands at high temperatures and high pressures, exhaust gas $\dot{V}_4[m^3/h]$ passes through a turbo, and an exhaust gas boiler heats water to produce steam needed for operations such as fuel preheating. Finally, the exhaust gas is discharged to the atmosphere at a temperature T_{in} downstream of the exhaust gas boiler. The waste heat recovery power generation system applied to this exhaust gas is described below.

First, to accurately measure the mass flow rate of the fuel consumed in the main engine, the mass flow rate being fed to the fuel injection system from the fuel storage tank and the mass flow rate returning to the fuel storage tank from the engine were measured, and the difference between their values was taken as the mass flow rate of the fuel being consumed in the main engine. The mass flow rates were measured by installing a Coriolis-type mass flow meter (Emerson Process Management, F-Series), which is precise to within ±0.1%, in the inlet and outlet piping of the fuel storage tank.

A torque measuring system (VAF Instruments, T-sense) was installed on a shaft coupling the main engine and a propulsion propeller, to measure both the torque [kN m] and rotational speed [rpm] of the propulsion shaft at a precision within ±0.5%. The shaft output $\dot{W}_{shaft}$ was found by conversion from these values. In addition, the temperature T_{in} downstream of the exhaust gas boiler was measured using an exhaust gas temperature sensor (Daeyang Instrument, MCA-D), which employs a SUS 304 protection tube and a k-type thermocouple. The ship speed was measured by GPS, and the data measured from each of the sensors was synchronized and saved with a sampling time of 5 min.

2.2. Operational profile of the main engine

The ship used in this experiment has a route with a repeating pattern passing through China's Ningbo–Shanghai, Korea's Kwangyang–Busan, and the U.S.'s Long Beach–Oakland in California, with one trip taking about two weeks. In the present study, data from a single one-way trip was used. Fig. 2 shows the data for the shaft output $\dot{W}_{shaft}$ with respect to the ship speed V_{ship}. The shaft output relative to the speed of this container ship has a correlation $\dot{W}_{shaft}[kW] = 13.541 \times V_{ship}^{2.499}$ [knot$^{2.499}$], and the correlation shows a value $R = 0.974$. Such results can be understood from the constant for the Admiralty coefficient C_A [16].

$$C_A = D_{ship}^{2/3} \times V_{ship}^{3} / \dot{W}_{shaft} \quad (1)$$

where D_{ship} represents the mass displacement of the ship. This signifies that the shaft output is inversely proportional to the third power of the ship speed, as $\dot{W}_{shaft} \sim V_{ship}^3$. Thus, the 2.499 power of the ship speed, which is the result of a regression analysis from the data measured in the present study, can be seen as a valid value, considering the conditions for low-speed operation from an engine load of an MCR of 50% or lower and the fluctuations in the resistance of the hull, depending on the size and shape of the hull and external forces.

Fig. 3 shows the mass flow rate $\dot{m}_f$ of the fuel consumed relative to the shaft output. This measured amount of HFO consumed has the property of typically being linearly proportional to the shaft output [17], and the best fit is $\dot{m}_f[t/h] = 0.19241 \times \dot{W}_{shaft}[MW]$ with $R = 0.997$. Here, the slope signifies the fuel consumption rate per unit power, which will be discussed in more detail later. This means that the ship speed and the container ship's fuel consumption rate investigated in the present study have a correlation $\dot{m}_f \sim V_{ship}^{2.499}$.

In Fig. 4, the closed circles indicate the probability distribution for the mass flow rate of the fuel consumed during travel along the ship's predetermined route. The probability distribution of the fuel consumption rate is defined as a value obtained by normalizing, as a percentage [%], the number of data sets exceeding a specific fuel consumption rate during operation of the ship over one-way, from the total number of the measured fuel consumption rates. A greater number of ranges with a high fuel consumption rate tended to result in a reduction in this probability distribution. In particular, in ranges A and B, indicated by the solid-line windows, the probability distribution for the fuel consumption rate showed relatively greater changes, which can be regarded as a steady interval of constant speed at which the ship was mainly driven. That is, in range A, where the mass flow rate of fuel was $2.0 \le \dot{m}_f$ [t/h] ≤ 2.5, the probability distribution represented about 13% of the total, at 91.08–78.15%. In range B, where the mass flow rate of fuel was $5.5 \le \dot{m}_f$ [t/h] ≤ 6.75, the probability distribution represented about 68.64% of the total, at 71.94–3.3%. Therefore, a combination of

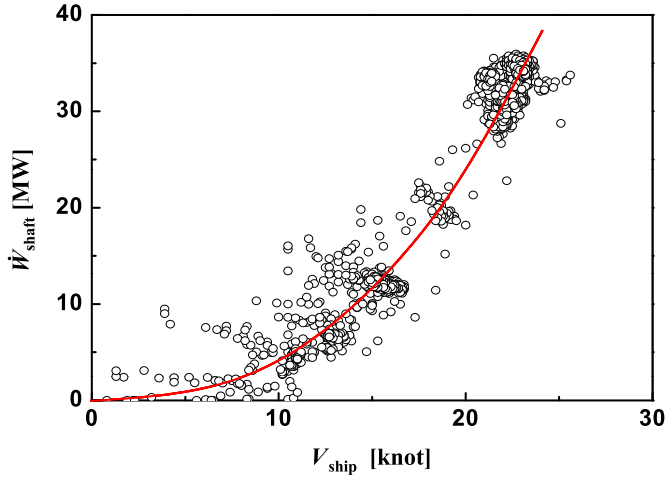

Fig. 2. Shaft power $\dot{W}_{shaft}$ as a function of ship speed V_{ship} during ship operation.

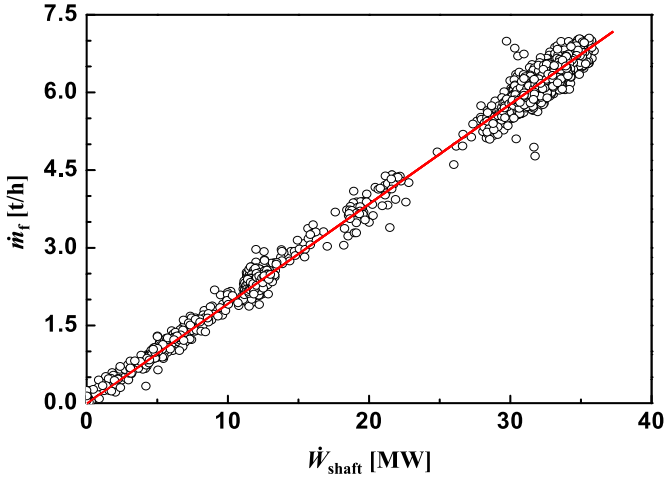

Fig. 3. Fuel mass flow rate $\dot{m}_f$ as a function of shaft power $\dot{W}_{shaft}$ during ship operation.

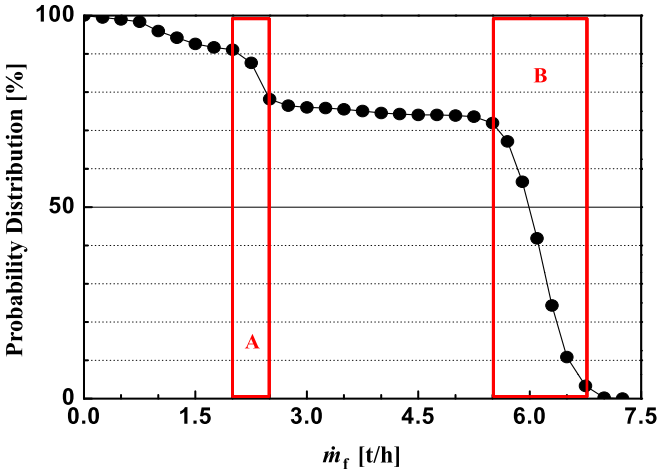

Fig. 4. Probability distribution of fuel mass flow rate $\dot{m}_f$ during ship operation.

ranges A & B shows that the steady intervals account for 81.64% during the entire travel. The range excluding ranges A & B, however, can be regarded as a transient interval, where the ship operated with either deceleration or acceleration.

In Fig. 5, the closed circles (left axis) indicate the probability distribution for the exhaust gas temperature with respect to the exhaust gas temperature downstream of the exhaust gas boiler during a one-way trip. A range C of $501 \leq T_{in}$ [K] ≤ 521, represented by the dashed-line window, has a power distribution that represents about 81% of the total, at 91.03–9.83%, with respect to the exhaust gas temperature. The open circles (right axis) indicate the data for the fuel consumption rate relative to the exhaust gas temperature. Ranges A and B represented by the solid-line windows in Fig. 4 are identically represented in Fig. 5 with solid-line windows. Thus, the dotted line stands for the two ranges of a 1st heat source and a 2nd heat source, where the A, B, and C window intersect, which are regarded as two representative ranges of primary operation for the ship's route.

2.3. Heat source of the exhaust gas

Specific heat source conditions for the exhaust gas, represented in Table 1, were selected one by one for the 1st and 2nd heat sources, which are the representative operating ranges for this ship.

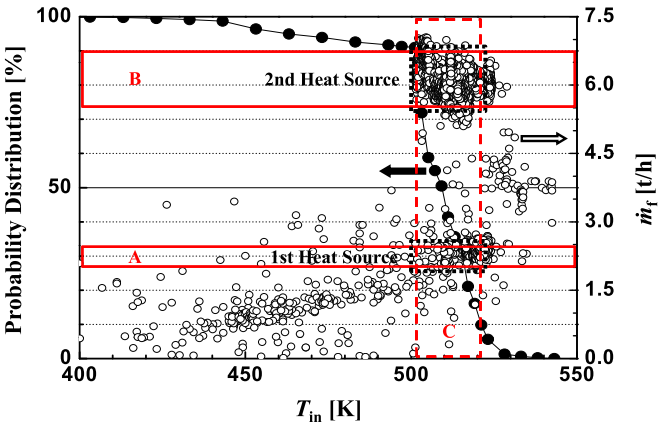

Fig. 5. Probability distribution of temperature T_{in} and fuel mass flow rate $\dot{m}_f$ for the temperature T_{in} at the outlet of exhaust gas boiler during ship operation.

Table 1
Two representative conditions for heat source of exhaust gas.

	1st heat source	2nd heat source
T_{in} [K]	510	
$C_{p,in}$ [kJ/kg K]	1.012	
$\dot{m}_f$ [kg/h]	2300	6100
f_C	53.8168	
Cal.$\dot{m}_{exh}$ [kg/h]	123,778.7	328,282.7
O_2 [%]	15.3	

In both cases, the representative gas temperature was fixed at one temperature, $T_{in} = 510$ K, and this was set as the average of the exhaust gas temperature data in the dashed-line window ranges in Fig. 5. The specific heat of exhaust gas has been assumed to approach the specific heat of air $C_{p,in} = 1.012$ kJ/kg K at normal temperatures and normal pressures [18]. The fuel consumption rate was selected at the arbitrary values of $\dot{m}_f = 2300$ and 6100 t/h, which are within the range of mass flow rates for ranges A and B in Fig. 4. In Table 1, the mass flow rate $\dot{m}_{exh}$ of the exhaust gas used values obtained by multiplying a conversion factor f_C by these selected fuel mass flow rates. f_C is calculated simply by the carbon balance method [19].

Assuming that the molecular formula of hydrocarbons in the heavy fuel oil being supplied to the main engine is $C_{30}H_{62}$ [20], and assuming that the fuel injected with the oxygen in the intaken air is entirely combusted inside the combustion chamber, the chemical equation is expressed by $C_{30}H_{62} + 45.5O_2 \rightarrow 30CO_2 + 31H_2O$ [21]. Based on this reaction formula, the mass ratio of CO_2 generated per kilogram of fuel is a value found by multiplying the mass ratio of C and CO_2 by the mass ratio of a C component contained in the fuel, as in MW (C_{30}/$C_{30}H_{62}$) × 30 MW (CO_2/C_{30}) = 0.853 × 3.667 = 3.128 $kg_{\_CO_2}/kg_{\_fuel}$. Here, MW (molecule) denotes the molecular weight. Assuming the purity of the fuel is 96.5% [20], the mass ratio of CO_2 generated per kilogram of fuel is 3.018 $kg_{\_CO_2}/kg_{\_fuel}$. Accordingly, the amount of oxygen required for the C component in 1 kg of this fuel to be combusted is 3.018−0.853 = 2.165 $kg_{\_O_2}/kg_{\_fuel}$, found by subtracting the mass of the C contained in 1 kg of fuel from the mass of CO_2 generated from 1 kg of fuel.

The mass ratio of H_2O generated per kilogram of fuel is found by multiplying the mass ratios of H_2O and H by the mass ratio of the H component contained in the fuel, as in MW (H_{62}/$C_{30}H_{62}$) × 62/2 MW (H_2O/H_{62}) = 0.14692 × 9 = 1.32228 $kg_{\_H_2O}/kg_{\_fuel}$. Thus, the amount of oxygen required in order for the H component in 1 kg of this fuel to combust is 1.32228−0.14692 = 1.17536 $kg_{\_O_2}/kg_{\_fuel}$, found by subtracting the mass of the H contained in 1 kg of fuel from the mass of H_2O generated from 1 kg of fuel.

The total amount of air needed for 1 kg of fuel to be combusted is (2.165 + 1.17536)/0.233 = 14.336 $kg_{\_air}/kg_{\_fuel}$, which is found by dividing the mass fraction of oxygen in the air by the amount of oxygen for combusting the C and H components in the fuel. Assuming that the oxygen concentration in the exhaust gas is 15.3% [15] and the oxygen concentration in the air is 21%, an excess air ratio of 15.3/(21−15.3) = 2.68421 can be considered. Thus, the actual mass of air fed to the combustion chamber of the engine has a value of 14.336 × (1 + 2.68421) = 52.8168 $kg_{\_air}/kg_{\_fuel}$, considering the excess air ratio in the total amount of air needed in order for 1 kg of fuel to be combusted.

Consequently, the mass ratio of the amount of 1 kg of fuel with respect to the value found by adding the amount of 1 kg of fuel and the total amount of air fed, at (52.8168 + 1)/1 = 53.8168 $kg_{\_exh}/kg_{\_fuel}$, is regarded as the total mass of exhaust gas discharged per kilogram of fuel. This value was defined as a conversion factor f_C, for calculating the mass flow rate of the exhaust gas from the mass flow rate of the fuel.

3. Thermodynamic model of the dual loop heat recovery system

Fig. 1 is a schematic of a waste heat recovery power generation system using a dual loop for exhaust gas of a 2-stroke diesel engine, utilized for the ship's main propulsion. The exhaust gas temperature of the main engine is defined as T_{in} and the mass flow rate is defined as $\dot{m}_{in}$. A 1–2–3–4 upper cycle using water as the working fluid was applied to the high-temperature part of the exhaust gas, and a 5–6–7–8–9 lower cycle using R1234yf as the working fluid was added to the low-temperature part, thus constituting a dual loop. The power generated by the upper and lower cycles of the waste heat recovery power generation system has been assumed to be a system recycled as propulsion power for the ship by complementing the shaft output of the engine with an electric motor [5].

3.1. Upper trilateral cycle

The maximum thermodynamic efficiency of a cycle driven through isentropic compression and expansion processes by the temperature differential between two heat storage tanks is also known as the Carnot efficiency [22–24]. In fact, because the temperature of a heat source while heat is being transmitted by a working fluid within a cycle from the heat source falls from a high temperature to a low temperature, a trilateral cycle from which the step of boiling the water working fluid is omitted can be regarded as a cycle that makes it possible to obtain the thermodynamically maximum efficiency for an actual heat source [25]. The upper cycle thus uses water, which is suitable for relatively high-temperature heat sources, as its working fluid. Saturated liquid water in a high-temperature, high-pressure state 3 adopts a trilateral cycle in which it is injected to a turbine 1, and expanded to a two-phase state of low-temperature, low-pressure steam and water, thus generating power. The thermodynamic equations for the steps in this cycle are as follows [22–24].

The consumed power $\dot{W}_{p1}$, efficiency η_{p1}, and exergy destruction rate $\dot{E}_{d,p1}$ of a pump 1 in process 1–2 are given in equations (2)–(4) below.

$$\dot{W}_{p1} = \dot{m}_{o1}(h_2 - h_1) \tag{2}$$

$$\eta_{p1} = (h_{2s} - h_1)/(h_2 - h_1) \tag{3}$$

$$\dot{E}_{d,p1} = \dot{m}_{o1} T_0 (s_2 - s_1) \tag{4}$$

$\dot{m}_{o1}$ is the mass flow rate of the working fluid water. h is the enthalpy [kJ/kg] and s is the entropy [kJ/kg K], per unit mass. The subscript 0 signifies a dead state where the exergy value is 0, assuming a normal temperature of $T_0 = 298.15$ K and a normal pressure of $P_0 = 101.3$ kPa.

In the case of process 2–3, the temperature of the exhaust gas discharged from the evaporator was defined as T_{out1}. Thus, the energy balance and destroyed exergy $\dot{E}_{d,e}$ inside the evaporator are as in equations (5) and (6) below, with respect to the amount of heat $\dot{Q}_e$ supplied from the heat sources.

$$\dot{Q}_e = \dot{m}_{o1}(h_3 - h_2) = \dot{m}_{in} c_{p,in}(T_{in} - T_{out1}) \tag{5}$$

$$\dot{E}_{d,e} = \dot{m}_{in}\{h_{in} - h_{out1} - T_0(s_{in} - s_{out1})\} + \dot{m}_{o1}\{h_2 - h_3 - T_0(s_2 - s_3)\} \tag{6}$$

where $C_{p,in}$ is the specific heat of a heat source.

The output $\dot{W}_{t1}$, efficiency η_{t1} and exergy destruction rate $\dot{E}_{d,t1}$ of a turbine 1 in process 3–4 are given in equations (7)–(9) below.

$$\dot{W}_{t1} = \dot{m}_{o1}(h_3 - h_4) \tag{7}$$

$$\eta_{t1} = (h_3 - h_4)/(h_3 - h_{4s}) \tag{8}$$

$$\dot{E}_{d,t1} = \dot{m}_{o1} T_0 (s_4 - s_3) \tag{9}$$

The remaining amount of heat $\dot{Q}_{re,t}$ is supplied in process 4–1 as the lower cycle from the upper cycle, through a regenerator, as in equation (10) below.

$$\dot{Q}_{re,t} = \dot{m}_{o1}(h_4 - h_1) \tag{10}$$

3.2. Lower organic Rankine cycle

Exhaust gas heat having a temperature T_{out1} discarded from the evaporator and heat remaining from downstream of the turbine 1 in the upper cycle are each recovered through a pre-heater and a regenerator in the lower cycle. Because this remaining waste heat source has a relatively low temperature, an ORC (organic Rankine cycle) using the organic working fluid R1234yf, which evaporates easily even in low-temperature heat sources, was applied to the lower cycle [26]. Note that R1234yf exhibits similar thermodynamic performance compared to R134a, and has been attracting attention as a next-generation alternative refrigerant, reducing the GWP (Global Warming Potential) to 4 [27]. However, the flammable limits of R1234yf have been expanded more so than the case of R134a, and the ignition temperature thereof is even lower, so the flammability is comparatively higher [28,29].

The thermodynamic equations for each of the processes in the lower cycle are represented below [23–25]. Firstly, the consumed power $\dot{W}_{p2}$, efficiency η_{p2}, and exergy destruction rate $\dot{E}_{d,p2}$ of a pump 2 in process 5–6 are given in equations (11)–(13) below.

$$\dot{W}_{p2} = \dot{m}_{o2}(h_6 - h_5) \tag{11}$$

$$\eta_{p2} = (h_{6s} - h_5)/(h_6 - h_5) \tag{12}$$

$$\dot{E}_{d,p2} = \dot{m}_{o2} T_0 (s_6 - s_5) \tag{13}$$

$\dot{m}_{o2}$ is the mass flow rate of the working fluid R1234yf.

In the case of process 6–7, the energy balance and exergy destruction rate $\dot{E}_{d,pr}$ inside the preheater are given in equations (14) and (15) below, for the amount of heat $\dot{Q}_{pr}$ fed from the temperature differential of the exhaust gas from T_{out1} to T_{out2}.

$$\dot{Q}_{pr} = \dot{m}_{o2}(h_7 - h_6) = \dot{m}_{in} c_{p,in}(T_{out1} - T_{out2}) \tag{14}$$

$$\dot{E}_{d,pr} = \dot{m}_{in}\{h_{out1} - h_{out2} - T_0(s_{out1} - s_{out2})\} + \dot{m}_{o2}\{h_6 - h_7 - T_0(s_6 - s_7)\} \tag{15}$$

The energy balance and exergy destruction rate $\dot{E}_{d,re}$ inside the regenerator are given in equations (16) and (17) below, for the amount of heat $\dot{Q}_{re,b}$ fed to the lower cycle from the regenerator in process 7–8.

$$\dot{Q}_{re,b} = \dot{m}_{o2}(h_8 - h_7) = \dot{m}_{o1}(h_4 - h_1) \tag{16}$$

$$\dot{E}_{d,re} = \dot{m}_{o1}\{h_4 - h_1 - T_0(s_4 - s_1)\} + \dot{m}_{o2}\{h_7 - h_8 - T_0(s_7 - s_8)\} \tag{17}$$

The output $\dot{W}_{t2}$, efficiency η_{t2}, and exergy destruction rate $\dot{E}_{d,t2}$ of the turbine 2 in process 8–9 are as in equations (18)–(20) below.

$$\dot{W}_{t2} = \dot{m}_{o2}(h_8 - h_9) \tag{18}$$

$$\eta_{t2} = (h_8 - h_9)/(h_8 - h_{9s}) \tag{19}$$

$$\dot{E}_{d,t2} = \dot{m}_{o2}T_0(s_9 - s_8) \tag{20}$$

The amount of heat $\dot{Q}_c$ discarded by a condenser and the exergy destruction rate $\dot{E}_{d,c}$ in process 9–5 are as in equations (21) and (22) below.

$$\dot{Q}_c = \dot{m}_{o2}(h_9 - h_5) \tag{21}$$

$$\dot{E}_{d,c} = \dot{m}_{o2}\{(h_9 - h_5) - T_0(s_9 - s_5)\} \tag{22}$$

3.3. Energy and exergy efficiency of the dual loop heat recovery system

The waste heat discarded by the exhaust gas of the ship's main engine is recovered from the dual loop heat recovery power generation system by an evaporator $\dot{Q}_e$ and a preheater $\dot{Q}_{pr}$. Thus, the cycle efficiency η_{cyc} for the first law of thermodynamics with respect to the net power produced by the difference in shaft work between turbines 1, 2 and pumps 1, 2 is given in equation (23) below.

$$\begin{aligned}\eta_{cyc} &= \left\{\left(\dot{W}_{t1} + \dot{W}_{t2}\right) - \left(\dot{W}_{p1} + \dot{W}_{p2}\right)\right\} \Big/ \left(\dot{Q}_e + \dot{Q}_{pr}\right) \\ &= \left(\dot{W}_{net1} + \dot{W}_{net2}\right) \Big/ \left(\dot{Q}_e + \dot{Q}_{pr}\right) = \dot{W}_{net} / \left(\dot{Q}_e + \dot{Q}_{pr}\right)\end{aligned} \tag{23}$$

The system efficiency η_{sys}, which takes into consideration the heat effectiveness, being the ratio of the maximum heat transfer rate $\dot{Q}_{max}$ that can be recovered through the evaporator and the preheater and the actual heat transfer rate $\dot{Q}_{act}$, is as given in equations (24) and (25) below [30].

$$\varepsilon = \dot{Q}_{act}/\dot{Q}_{max} = (T_{in} - T_{out2})/(T_{in} - T_5) \tag{24}$$

$$\eta_{sys} = \varepsilon\,\eta_{cyc} \tag{25}$$

In turn, the heat source exergy rate $\dot{E}_{in}$ and destroyed exergy rate $\dot{E}_{out2}$ are as given in equations (26) and (27) below.

$$\dot{E}_{in} = \dot{m}_{in}\{h_{in} - h_0 - T_0(s_{in} - s_0)\} \tag{26}$$

$$\dot{E}_{out2} = \dot{m}_{in}\{h_{out2} - h_0 - T_0(s_{out2} - s_0)\} \tag{27}$$

Thus, for the waste heat recovery power generation system using this dual loop scheme, the exergy efficiency η_e for the second law of thermodynamics, with respect to the exergy rate supplied by the cycle and the exergy rate utilized in the system is as given in equation (28) below.

$$\eta_e = \dot{W}_{net}/\dot{E}_{in} = \left(\dot{E}_{in} - \Sigma\dot{E}_d - \dot{E}_{out2}\right) \Big/ \dot{E}_{in} \tag{28}$$

The exergy effectiveness ε_e, being the ratio for the maximum usable exergy rate and the actually transmitted exergy rate, and the system exergy efficiency $\eta_{sys,e}$ taking this exergy effectiveness into consideration are as given in equations (29) and (30) below [30].

$$\varepsilon_e = \left(\dot{E}_{in} - \dot{E}_{out2}\right) \Big/ \dot{E}_{in} \tag{29}$$

$$\eta_{sys,e} = \varepsilon_e\eta_e \tag{30}$$

3.4. Calculation conditions

Table 2 summarizes the thermodynamic property conditions for the working fluids water and R1234yf, used for the thermodynamic calculations for the exhaust gas heat recovery power generation system using the dual loop. First, qualities X_1 and X_5 of the working fluids at the inlets of pumps 1 and 2 were fixed to zero (as the ratio of the mass of vapor to the total mass of the mixture), and the efficiencies of both pumps $\eta_{p1,2}$ and turbines $\eta_{t1,2}$ were fixed to 0.85. The critical pressure P_c corresponding to the critical temperature T_c of each working fluid was set as the maximum pressure P_{max}. Taking into consideration the maximum temperature of the seawater in terms of the design of the ship, the minimum temperature T_{min} of the lower cycle and the inlet temperature T_5 for the pump 2 were both fixed to 305 K [31]. The corresponding pressure P_5 was set as the minimum pressure P_{min} of the lower cycle.

In particular, the minimum temperature T_{min} and the minimum pressure P_{min} for the upper cycle, which is the boundary between the upper cycle and the lower cycle, were set as the temperature T_1 and pressure P_1 in state 1. A pinch point temperature difference ΔT_{pp1}, which has a minimum temperature difference with the heat source in the upper cycle, was defined as the difference between temperature T_{in} of the heat source and temperature T_3 of state 3, which is a saturated liquid [32]. A lower pinch point temperature difference ΔT_{pp2} was defined as the temperature difference between the lowest temperature of the upper cycle ($T_1 = T_4$) and a temperature T_7 in a state 7 of the lower cycle, and was fixed to 10 K in order to eliminate the effects with respect to changes in the ΔT_{pp2}.

The dimensionless turbine inlet pressure and mass flow rate ratio for the working fluids were defined according to equations (31)–(34) given below.

$$R_{p1} = (P_2 - P_1)/(P_{c1} - P_1) \tag{31}$$

$$R_{p2} = (P_6 - P_5)(P_{c2} - P_5) \tag{32}$$

$$R_{m1} = \dot{m}_{o1}/\dot{m}_{in} \tag{33}$$

$$R_{m2} = \dot{m}_{o2}/\dot{m}_{in} \tag{34}$$

The upper cycle was fixed to (R_{m1}, R_{p1}) = (0.12, 0.12) for the working fluid, in order to form a trilateral cycle. In addition, to eliminate the impact of flow rate changes for the organic working fluid in the lower organic Rankine cycle, the mass flow rate ratio was fixed to $R_{m2} = 1$. The pressure R_{p2} was allowed to fluctuate owing to changes in the critical temperature (T_1) of the dual loop. These thermodynamic calculations were carried out using EES ver. 8 [33].

Table 2
Thermodynamic conditions for water (TC) and R1234yf (ORC) cycles of the dual loop heat recovery system.

	Water (TC)	R1234yf (ORC)
T_c [K]	647.1	367.9
P_{max} [MPa]	$P_{c1} = 22.062$	$P_{c2} = 3.38$
T_{min} [K]	T_1	$T_5 = 305$
P_{min} [kPa]	P_1	$P_5 = 823.4$
X_1, X_5	0	0
ΔT_{pp} [K]	$\Delta T_{pp1} = T_{in} - T_3$	$\Delta T_{pp2} = T_1 - T_7 = 10$
η_{p1}, η_{p2}	0.85	0.85
η_{t1}, η_{t2}	0.85	0.85
R_m	$R_{m1} = \dot{m}_{ol}/\dot{m}_{in} = 0.12$	$R_{m2} = \dot{m}_{ol}/\dot{m}_{in} = 1$
R_p	$R_{p1} = (P_2 - P_1)/(P_{c1} - P_1) = 0.12$	$R_{p2} = (P_6 - P_5)/(P_{c2} - P_5)$

4. Results and discussion

The properties of exhaust gas discharged from the main engine of the actually operating container ship were analyzed above. As a result, an exhaust gas heat recovery power generation system with a dual loop was theoretically applied to representative heat sources of the selected 1st heat source and the 2nd heat source (Table 1).

The thermodynamic properties of the upper and lower cycles depending on changes in the critical temperature $T_1 = 320–375$ K are investigated below with respect to the heat source of the 2nd heat source, and the energy and exergy efficiencies of the waste heat recovery cycles of the dual loop were studied. The case of the 1st heat source is also discussed, by carrying out calculations using the same procedure and only applying the resulting values.

4.1. Thermodynamic characteristics of the upper trilateral cycle

Fig. 6 illustrates a typical T–s diagram for the dual loop waste heat recovery cycle, which comprises the upper TC (trilateral cycle) and the lower organic Rankine cycle (ORC) defined in the present study. Firstly, the thermodynamic characteristics of the single loop trilateral cycle and the dual loop cycle are compared in Fig. 6a, for a fixed condensation temperature of the upper cycle at $T_1 = 305$ K; in this figure, each of the states (T [K], s [kJ/kg K]) of the single loop trilateral cycle for the saturated liquid line of water is represented with a dashed line. Further, the representative thermodynamic properties of the single and dual loop are listed in Table 3. The upper cycle of the single loop is constituted of $(T_1, s_1) = (305, 0.462)$, $(T_2, s_2) = (305.2, 0.4635)$, the turbine 1 inlet conditions for the saturated liquid state $(T_3, s_3) = (500.4, 2.583)$, and the vapor-and-liquid two-phase state $(T_4, s_4) = (305, 2.68)$. This is in the form of a typical trilateral cycle, omitting the process of boiling the water, which is the working fluid in an ordinary Rankine cycle [32].

In Fig. 6b, at $T_1 = 320$ K, each of the states (T [K], s [kJ/kg K]) of the upper cycle for the dual loop is constituted of $(T_1, s_1) = (320, 0.6628)$, $(T_2, s_2) = (320.2, 0.6642)$, the turbine 1 inlet conditions for the saturated liquid state $(T_3, s_3) = (500.4, 2.584)$, and the vapor-and-liquid 2-phase state $(T_4, s_4) = (320, 2.662)$. This form of the upper trilateral cycle for the dual loop including the lower organic Rankine cycle is similar to that of the single loop trilateral cycle.

In Fig. 6c, when $T_1 = 375$ K, each of the states (T [K], s [kJ/kg K]) of the upper cycle for the dual loop is constituted of $(T_1, s_1) = (375, 1.328)$, $(T_2, s_2) = (375.3, 1.329)$, $(T_3, s_3) = (502.1, 2.6)$, and $(T_4, s_4) = (375, 2.633)$. When the boundary temperature T_1 of the upper and lower cycles rises, the graph of T–s had a reduced interior area with respect to the path for each of the steps of the trilateral cycle.

To better understand the thermodynamics for the dual loop, Fig. 7 shows the exhaust gas temperatures T_{out1} and T_{out2} for different changes in $T_1 = 320–375$ K, the pinch point temperature differential ΔT_{pp1}, and the amount of heat $\dot{Q}$ recovered or released from each heat exchanger. When the inlet temperature for the pump 1 was boosted to $T_1 = 375$ K, because the amount of heat recovered from the evaporator was reduced to $\dot{Q}_e = 6078.1$ kW, the exhaust gas outlet temperature increased to $T_{out1} = 444.2$ K. Accordingly, the amount of heat transmitted from the upper cycle to the lower cycle through the regenerator reduced to $\dot{Q}_r = 5,358.0$ kW. Note that when the pinch point temperature differential between T_{in} and T_3 is slightly decreased, at $\Delta T_{pp1} = 9.616–7.893$ K, it was almost constant.

Fig. 8 shows the inlet/outlet volumetric flow rate and volumetric expansion ratio for the turbines 1 and 2 depending on changes in the boundary temperature T_1. First, the working fluid of the trilateral cycle expanded to a state of a mixture of vapor and liquid from a saturated liquid state at $T_1 = 320$ K in the trilateral upper cycle, and therefore, the volumetric expansion ratio for the turbine 1 appeared to be excessively large, at $\dot{V}_4/\dot{V}_3 = 3111.98$. In addition, as T_1 was varied in the range 320–375 K, the turbine 1 inlet volumetric flow rate was kept substantially constant at $\dot{V}_3 = 47.41–47.54$ m^3/h, whereas the turbine outlet volumetric flow rate was sharply reduced to $\dot{V}_4 = 147,539–13,519$ m^3/h. Consequently, the volumetric expansion ratio for the turbine 1

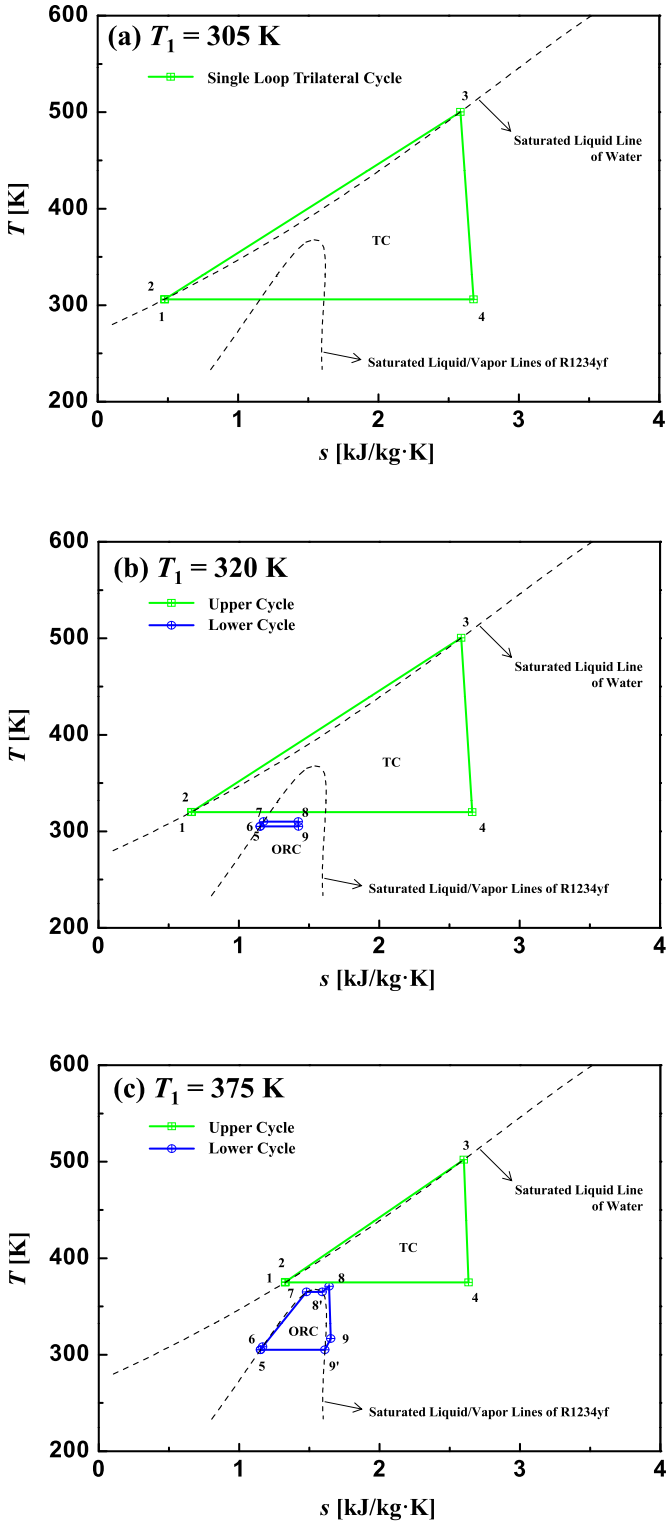

Fig. 6. T-s diagram for (a) single loop of the upper cycle (TC) at $T_1 = 305$ K and for dual loop of the upper (TC) and the lower (ORC) cycles at (b) $T_1 = 320$ K and (c) $T_1 = 375$ K.

Table 3
Representative thermodynamic data of single loop trilateral cycle at $T_1 = 305$ K and dual loop cycles at both $T_1 = 320$ and 327 K.

		Single loop		Dual loop			
		$T_1 = 305$ K		$T_1 = 320$ K		$T_1 = 375$ K	
T_1 [K]	s_1 [kJ/kg K]	305	0.462	320	0.6628	320	0.6628
T_2 [K]	s_2 [kJ/kg K]	305.2	0.4635	320.2	0.6642	320.2	0.6642
T_3 [K]	s_3 [kJ/kg K]	500.3	2.583	500.4	2.584	500.4	2.584
T_4 [K]	s_4 [kJ/kg K]	305	2.68	320	2.662	320	2.662
T_5 [K]	s_5 [kJ/kg K]	–	–	305	1.152	305	1.152
T_6 [K]	s_6 [kJ/kg K]	–	–	305.1	1.152	308.2	1.167
T_7 [K]	s_7 [kJ/kg K]	–	–	310	1.175	365	1.48
$T_{8'}$ [K]	$s_{8'}$ [kJ/kg K]	–	–	–	–	365	1.592
T_8 [K]	s_8 [kJ/kg K]	–	–	310	1.423	371	1.641
T_9 [K]	s_9 [kJ/kg K]	–	–	305	1.424	305	1.652
$T_{9'}$ [K]	$s_{9'}$ [kJ/kg K]	–	–	–	–	305	1.611
T_{out1} [K]		410.4		417.8		444.2	
T_{out2} [K]		–		410.6		336.6	
ΔT_{pp1} [K]		9.7		9.616		7.893	
$\dot{Q}_e$[kW]		9200		8518.1		6078.1	
$\dot{Q}_r$[kW]		–		7006.2		5358.0	
$\dot{Q}_{pr}$[kW]		–		660.4		9,938.5	
$\dot{Q}_c$[kW]		7408		7571.2		13,944.9	
$\dot{V}_3$[m^3/h]		47.4		47.41		47.54	
$\dot{V}_4$[m^3/h]		327,219		147,539		13,519	
$\dot{V}_g/\dot{V}_3$		6903.35		3111.98		284.37	
$\dot{V}_g$[m^3/h]		–		3,662		1,402	
$\dot{V}_9$[m^3/h]		–		4363		7678	
$\dot{V}_9/\dot{V}_g$		–		1.191		5.476	

when $T_1 = 375$ K was reduced by about 11-fold, at $\dot{V}_4/\dot{V}_3 = 284.37$, in comparison to the value from when $T_1 = 320$ K. The quality of the turbine 1 outlet, then, was in the range $X_4 = 0.2678–0.2173$ for this T_1, and therefore, the application of a positive displacement expander capable of normal operation even for a low-quality 2-phase working fluid of a steam–water mixture should be considered [34].

In particular, in the case of the single loop trilateral cycle at $T_1 = 305$ K (Table 3), the volumetric expansion ratio for the turbine was $\dot{V}_4/\dot{V}_3 = 6903.35$. Thus, when the organic Rankine cycle is added as a bottom cycle to the trilateral cycle and the boundary temperature T_1 of the upper and lower cycles in the dual loop increases, the volumetric expansion ratio of turbine 1 in the trilateral cycle can be reduced considerably, thus signifying that the volume and weight of the positive displacement could be scaled down.

4.2. Thermodynamic characteristics of the lower organic Rankine cycle

In Fig. 6b, with the lower cycle maintaining $T_1 = 320$ K, the working fluid R1234yf cannot be adequately heated to a gaseous state from the saturated liquid state, and therefore, a 2-phase state of vapor and liquid was observed in the states 8 and 9 of the turbine 2 inlet/outlet.

However, in Fig. 6c, with $T_1 = 327$ K, the lower cycle constituted a typical organic Rankine cycle. That is, from $(T_5, s_5) = (305, 1.152)$ and $(T_6, s_6) = (308.2, 1.167)$, the ($T$ [K], s [kJ/kg K]) for each of the states at the pump 2 inlet/outlet, through to a saturated liquid state 7 of $(T_7, s_7) = (365, 1.48)$ and a saturated vapor state 8′ of $(T_{8'}, s_{8'}) = (365, 1.592)$, the turbine 2 inlet was successfully heated to a superheated vapor state 8, at $(T_8, s_8) = (371, 1.641)$. This is because, as shown in Fig. 7, the increase in T_1 was accompanied by a rapid increase in the amount of heat transmitted to the preheater of the lower cycle from the heat source, to $\dot{Q}_{pr} = 9938.5$ kW. In contrast, the temperature of the exhaust gas finally discarded downstream of the preheater was lowered to $T_{out2} = 336.6$ K. The thermodynamic data for both conditions of $T_1 = 320$ and 327 K in the dual loop cycle are also listed in Table 3. This means that heat loss to the heat source was minimized by the increase in the temperature of T_1, which is the boundary temperature of the upper and lower cycles in the dual loop; a more detailed explanation of this will follow, through an exergy analysis.

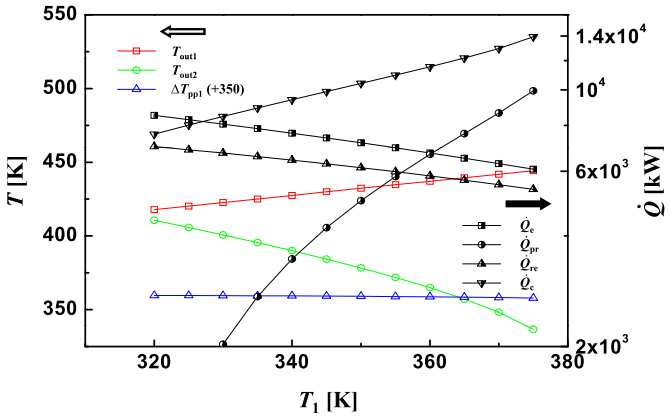

Fig. 7. Characteristics of certain temperatures and heat transfer when T_1 is varied.

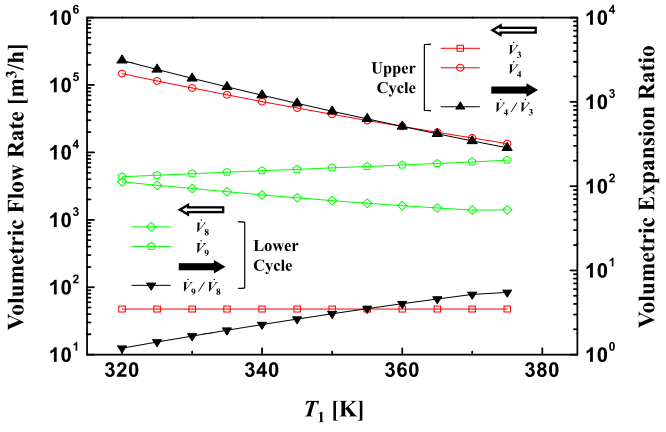

Fig. 8. Volume flow rate and volume expansion ratio at the inlet/outlet of the expanders when T_1 is varied.

Note that, in general, R134a refrigerant is known to be a non-flammable gas in normal-temperature and normal-pressure air [28]. Under conditions of elevated temperature and pressure of the air, the refrigerant is more easily ignited; in particular, R134a has been shown to be flammable in air having normal pressure at 553 K [35]. In addition, R1234yf is also classified as a mildly flammable gas in normal-temperature normal-pressure air, too, and an elevation in the temperature and humidity of the air has been shown to result in an expansion of the flammable limits [36]. Thus, in the present study, because the exhaust gas temperature after the evaporator was increased to $T_{out1} = 444.2$ K depending on a boundary temperature of T_1 and moisture was actually included, the R1234yf could leak and come into contact with the exhaust gas, resulting in the risk of fire. During combustion, the toxic substance HF (hydrogen fluoride) is produced [37], so ventilation equipment must also be considered to combat the occurrence of fire. Although a non-combustible heat transfer medium, such as water, between the exhaust gas and R1234yf could also be used, the system efficiency might be reduced. However, the exhaust gas after having been combusted in the engine has an oxygen concentration of about 15% and, therefore, might also have a reduced flammability in comparison to the 21% oxygen ratio of general air. The fire safety of R1234yf thus requires future research.

In addition, when the temperature of the exhaust gas falls below the acid dew point temperature for emissions such as SO_x and NO_x contained in the exhaust gas, the moisture is condensed in conjunction to acids such as sulfuric and nitric acid, which causes corrosion of the heat exchangers. Therefore, it is necessary for the design to allow the temperature of the exhaust gas being discharged to the atmosphere to be higher than this acid dew point [38]. However, in the present study, the low-temperature corrosion was prevented through the application of various technologies, such as low-sulfur fuel oil conversion or heat exchangers made of anti-corrosive materials, and hence, we did not set a limit point for the lowest temperature with respect to the exhaust gas temperature T_{out2} downstream of the preheater.

In contrast, for the expansion process 8–9 in the lower organic Rankine cycle, in Fig. 8 the quality of the working fluid at the turbine 2 inlet/out increased to 1 in association with the increase $T_1 = 320$–375 K, and the volumetric flow rate of the turbine inlet/outlet was reduced and increased, to $\dot{V}_8 = 3662$–1402 m^3/h and $\dot{V}_9 = 4363$–7678 m^3/h, respectively. Consequently, at $T_1 = 375$ K, in Fig. 6c, the volumetric expansion ratio of the turbine 2 showed a maximum value of $\dot{V}_9/\dot{V}_8 = 5.476$, and during the expansion process 8–9, the turbine's outlet maintained a superheated vapor state. This accordingly signifies that over the leading T–s, the lower organic Rankine cycle using the R1234yf, which is a dry fluid having a slope of $dT/ds > 0$ relative to the line for the saturated vapor, operated while avoiding the 2-phase range of liquid–vapor, and therefore, a decline in output or damage during turbine usage could be prevented [39].

Note that the cooling process in 9(-9′)-1 showed a characteristic wherein, as shown in Fig. 7, the increase in T_1 was accompanied by an increase in the amount of heat recovered by the preheater, but the amount of heat discharged through the condenser also simultaneously increased to $\dot{Q}_c = 13,944.9$ kW. Accordingly, for a better understanding of the performance properties of the dual loop combined cycles along this increase in T_1, the analysis is carried out with the first and second laws of thermodynamics.

4.3. The energy and exergy efficiency of the dual loop heat recovery system

Fig. 9 shows the energy (a) and exergy (b) properties with respect to changes in the boundary temperature for this dual loop

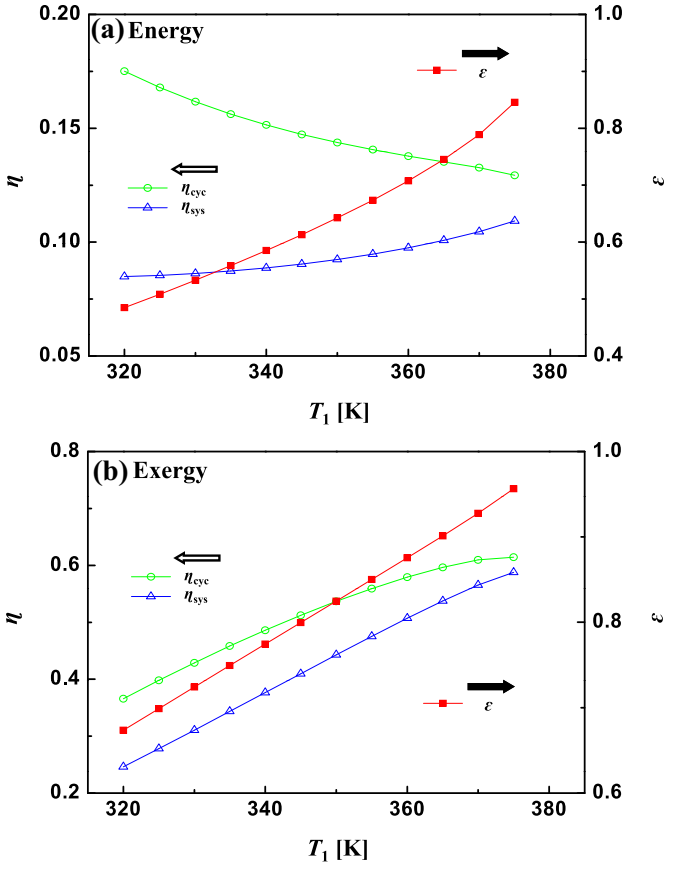

Fig. 9. Characteristics of efficiency η and effectiveness ε of (a) energy and (b) exergy when T_1 is varied.

waste heat recovery power generation system. First, in Fig. 9a, the cycle efficiency was reduced with the increase to $T_1 = 320$–375 K. This reflects the result where the amount of heat $\dot{Q}_{pr}$ recovered through the preheater had a relatively large increase. In addition, because this recovered heat causes an increase in the amount of heat $\dot{Q}_{act}$ actually recovered from the heat sources, the heat effectiveness ε was improved steadily as T_1 increased, resulting in a tendency for the system efficiency to also be elevated. Accordingly, with $T_1 = 375$ K, system efficiency was maximum at $\eta_{sys} = 0.1093 (= 10.93\%)$, with respect to the heat effectiveness $\varepsilon = 0.8457$ and cycle efficiency of $\eta_{cyc} = 0.1293 (= 12.93\%)$.

However, in Fig. 9b, the increase in T_1 was accompanied by a tendency for increase in the exergy effectiveness, exergy efficiency, and system exergy efficiency. Thus, with $T_1 = 375$ K, system exergy efficiency had a peak value of $\eta_{sys,e} = 0.5877$ (=58.77%), with respect to an exergy effectiveness of $\varepsilon_e = 0.9564$ and an exergy efficiency of $\eta_e = 0.6145$ (=61.45%). To analyze the cause for this, the exergy properties of the dual loop heat recovery system according to changes in T_1 were analyzed.

Fig. 10 shows the properties of the heat source exergy rate $\dot{E}_{in}$, total exergy destruction rate $\sum \dot{E}_d$, exergy efficiency $\dot{E}_{out2}$, and net output $\dot{W}_{net}$ for the change $T_1 = 320$–375 K. First, the heat source exergy rate had a constant value at $\dot{E}_{in} = 4821$ kW, for the exhaust gas of the 2nd heat source. In contrast, with the increase in the temperature T_1, as was discussed earlier, the amount of heat recovered from the heat sources increased, because of the increase in the lower cycle's performance, and the heat loss rate showed a tendency to reduce, at $\dot{E}_{out2} = 1573$–210.4 kW. This resulted in the increase in the exergy effectiveness in accordance with T_1, as shown in Fig. 9b.

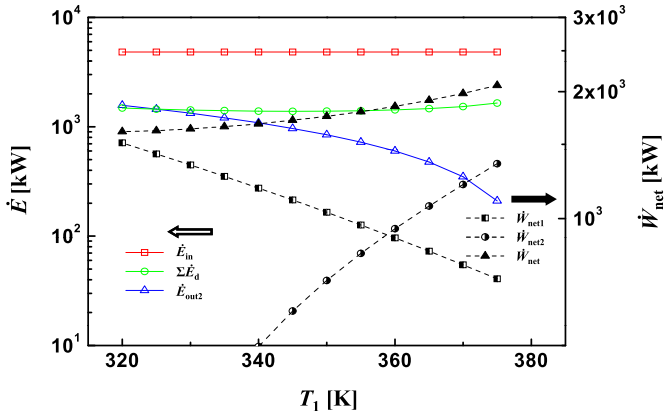

Fig. 10. Total exergy destruction rate $\sum \dot{E}_d$, exergy rate $\dot{E}_{in}$ of heat source, exergy loss rate $\dot{E}_{out2}$, and net work rates $\dot{W}_{net}$ when T_1 is varied.

Fig. 10 shows that although the net output of the upper cycle was reduced to $\dot{W}_{net1}$ = 1512–719.8 kW in accordance with the increase in T_1, the lower cycle net output was increased, to $\dot{W}_{net2}$ = 95.19–1350 kW. Consequently, the net output of the dual loop power generation system, represented by the sum of each of the outputs for the upper and lower cycles, exhibited a tendency to increase to $\dot{W}_{net}$ = 1607.19–2069.8 kW. This results in the increase in the exergy efficiency in accordance with T_1, as shown in Fig. 9b. Thus, because the exergy effectiveness and the exergy efficiency increased simultaneously according to T_1, the exergy efficiency of the system also can be understood to have increased according to T_1, as shown in Fig. 6b.

Fig. 10 shows that although the sum $\sum \dot{E}_d$ of the rate of exergy destroyed in each of the components inside the dual loop held constant overall, there was the probably of a slight decrease in accordance with an increase in T_1. To better understand this, Fig. 11 examines the properties of the heat exchangers and the exergy destruction rate for the pump and turbine with respect to the change in T_1 = 320–375 K.

For the upper cycle, the exergy destruction rate $\dot{E}_{d,e}$ in the evaporator was reduced, at 813.6–378 kW, and the exergy destruction rate $\dot{E}_{d,r}$ = 210.6–107.3 kW inside the regenerator was also reduced, in accordance with the increase in T_1. Moreover, the exergy destruction rate in the turbine 1 and the exergy destruction rate in the pump were also reduced, at

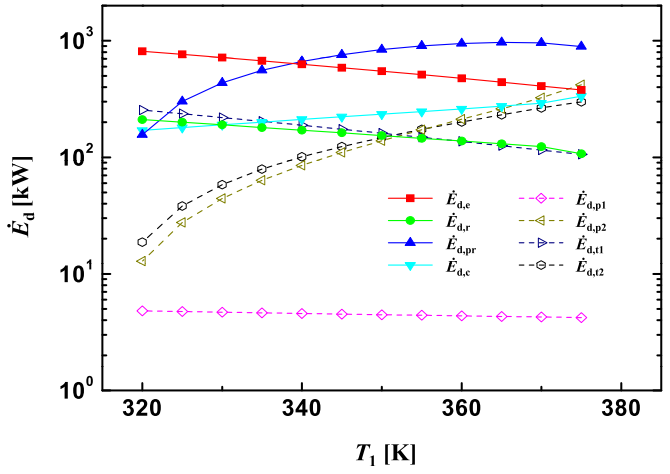

Fig. 11. Exergy destruction rates $\dot{E}_d$ of heat exchangers, pumps, and expanders when T_1 is varied.

$\dot{E}_{d,t1}$ = 254.2–106 kW and $\dot{E}_{d,p1}$ = 4.811–4.224 kW, respectively. This signifies that because of the reduction in the temperature differential between the heat source temperature and the lowest temperature of the upper cycle, the amount of heat $\dot{Q}_e$ supplied through the evaporator is reduced, and the energy deviation in the upper cycle reduced overall.

With the lower cycle, however, the exergy destruction rate $\dot{E}_{d,pr}$ in the preheater was increased, at 156.2–892.4 kW, as was the exergy destruction rate in the condenser $\dot{E}_{d,c}$ = 170.1–334.4 kW. In addition, the exergy destruction rate in the pump 2 and the turbine 2 also showed a tendency to increase, at $\dot{E}_{d,p2}$ = 12.87–419.8 kW and $\dot{E}_{d,t2}$ = 18.73–298.6 kW, respectively. This is because the amount of heat supplied from the preheater increased in accordance with the increase in T_1, and thus, the maximum and minimum temperature differential inside the lower cycle showed a corresponding increase. Thus, Fig. 10 demonstrates that the non-monotonic properties of the sum $\sum \dot{E}_d$ of the exergy destruction rate in accordance with T_1 result in a counterbalance between the contradictory properties of the exergy destruction rate for the configurations inside the upper and lower cycles, with respect to T_1.

Note that the entire data for T_1 = 320 and 327 K (Figs. 9–11) for the dual loop as well as the data for T_1 = 305 K for the single loop are listed in Table 4. These data indicate that the energy and exergy efficiencies of the dual loop system consist of the upper trilateral cycle and the lower organic Rankine cycle, which, as suggested in the present study, were larger than those of the single loop trilateral cycle. That is, for the single loop trilateral cycle, the system efficiency had η_{sys} = 0.09472 (=9.472%), with respect to the heat effectiveness ε = 0.4863 and cycle efficiency of η_{cyc} = 0.1948 (=19.48%). Besides, the system exergy efficiency had $\eta_{sys,e}$ = 0.2508 (=25.08%), with respect to the exergy effectiveness of ε_e = 0.6749 and exergy efficiency of η_e = 0.3717 (=37.17%).

4.4. Reduction of SFOC (Specific Fuel Oil Consumption) and CO_2 emission

As shown in the schematic (Fig. 1) of the waste heat recovery power generation system applied to the exhaust gas of the 2-stroke diesel engine of the ship, the chemical energy of the fuel supplied to

Table 4
Data for energy and exergy efficiencies of single loop trilateral cycle at T_1 = 305 K and dual loop cycles at both T_1 = 320 and 327 K.

	Single loop	Dual loop	
	T_1 = 305 K	T_1 = 320 K	T_1 = 375 K
ε	0.4863	0.4848	0.8457
η_{cyc}	0.1948	0.1751	0.1293
η_{sys}	0.09472	0.08487	0.1093
ε_e	0.6749	0.6737	0.9564
η_e	0.3717	0.3657	0.6145
$\eta_{sys,e}$	0.2508	0.2463	0.5877
$\dot{E}_{in}$ [kW]	4821	4821	4821
$\dot{E}_{out2}$ [kW]	1567	1573	210.4
$\dot{W}_{net1}$ [kW]	–	1512	719.8
$\dot{W}_{net2}$ [kW]	–	95.19	1350
$\dot{W}_{net}$ [kW]	1792	1607.2	2069.8
$\sum \dot{E}_d$ [kW]	1462	1485	1648
$\dot{E}_{d,e}$ [kW]	975.6	813.6	378
$\dot{E}_{d,r}$ [kW]	–	210.6	107.3
$\dot{E}_{d,t1}$ [kW]	315	254.2	106
$\dot{E}_{d,p1}$ [kW]	5.021	4.811	4.224
$\dot{E}_{d,pr}$ [kW]	–	156.2	892.4
$\dot{E}_{d,c}$ [kW]	166.4	170.1	334.4
$\dot{E}_{d,p2}$ [kW]	–	12.87	419.8
$\dot{E}_{d,t2}$ [kW]	–	18.73	298.6

the main engine is converted by the internal combustion engine to the mechanical kinetic energy of the shaft output $\dot{W}_{shaft}$. The heat energy of the exhaust gas discharged from the main engine is converted to electrical energy by the dual loop waste heat recovery power generation system. The net power $\dot{W}_{net}$ generated ultimately will serve as the propulsion power $\eta_{propulsion} = 0.44412$, being used as a secondary power to the main engine's shaft output. Thus, assuming no loss during transfer of the power generated by the waste heat recovery power generation system to the propulsion shaft, the conversion efficiency for the total propulsion output of the ship relative to the chemical energy of the fuel can be defined as the propulsion efficiency $\eta_{propulsion}$ in equation (35) below [40].

$$\eta_{propulsion} = \left(\dot{W}_{shaft} + \dot{W}_{net}\right) \Big/ \dot{m}_f \mathrm{LHV} = \dot{W}_{propulsion} / \dot{m}_f \mathrm{LHV} \tag{35}$$

The fuel is assumed to be DMC grade Bunker-A specified in ISO 8217 and the lower heating value is assumed to LHV = 10,063 kcal/kg [15].

In this regard, data for the propulsion power of the main engine is shown in Fig. 12, as the LHV term $\dot{m}_f$. As a result, the data measured from the actually operating ship is represented by open circles, and data for the base engine showed a linear correlation $\dot{W}_{propulsion} (= \dot{W}_{shaft}) = 0.44412 \times \dot{m}_f$ LHV. Herein, there was a correlation $R = 0.997$. Conversely, closed squares in Fig. 12 indicate the data for the main engine using the exhaust gas heat recovery power generation system, with regard to the two representative exhaust gas heat sources described above. For these two points, a linear correlation $\dot{W}_{propulsion} = 0.47236 \times \dot{m}_f$ LHV with $R = 1$. Thus, Fig. 12 shows that the slope values signify the propulsion efficiency, so depending on whether or the waste heat recovery system is being applied to the main engine, there was a propulsion efficiency of $\eta_{propulsion} = 0.44412$ (=44.412%) and 0.47236 (=47.236%). This means that in comparison to the case of a base engine on the basis of the energy of the fuel in an actually operating ship, this waste heat recovery system offers a 2.824% improvement in propulsion efficiency.

Furthermore, the SFOC (Specific Fuel Oil Consumption) defined as the mass flow rate of the fuel consumed per unit propulsion power in the main engine is given in equation (36) below [40].

$$\mathrm{SFOC}\left[\mathrm{g_{-fuel}/kWh}\right] = \dot{m}_f / \dot{W}_{propulsion} \tag{36}$$

In this regard, open circles in Fig. 13 indicate the fuel consumption rate consumed relative to the propulsion output in the ship's main engine. Based on this result, the base engine has a linear correlation $\dot{m}_f = 0.19241 \times \dot{W}_{propulsion}$ with $R = 0.997$. In addition, with regard to the two points of the closed squares illustrating the case where the exhaust gas heat recovery system was applied to the engine, there was a correlation of $\dot{m}_f = 0.18075 \times \dot{W}_{propulsion}$ with $R = 1$. In Fig. 13, the slope values signify the SFOC of the main engine. Thus, as was explained above, this signifies an effect wherein the improved propulsion efficiency from the waste heat recovery power generation system caused a 6.06% reduction in the SFOC of the actually operating ship's main engine, from 192.4 to 180.75 $g_{\_fuel}$/kWh.

Moreover, the value found by multiplying the fuel consumption rate per unit power by the mass ratio of CO_2 generated per kilogram of fuel, as mentioned above, can be regarded as the main engine's SCE (Specific CO_2 Emission) [$g_{\_CO_2}$/kWh] [20]. Therefore, the SCE for the base engine and the engine using the exhaust gas heat recovery system is $SCE_{\_Base} = 580.6934$ $g_{\_CO_2}$/kWh and $SCE_{\_EG\text{-}HRS} = 545.5035$ $g_{\_CO_2}$/kWh, respectively. Consequently, this signifies that the amount of fuel conserved by the waste heat recovery system for the exhaust gas can result in reduction in specific CO_2 emissions of approximately SCE = 35.19 $g_{\_CO_2}$/kWh, in contrast to the base engine during ship operation.

The error analysis was additionally performed for determining the difference in the assumed thermodynamic properties such as the heat source and the efficiencies of pumps and turbines in the dual loop waste heat recovery system with $T_1 = 327$ K; the results are listed in Table 5. Based on the reference value for $T_1 = 327$ K, as explained previously, when $C_{p,in}$ for the exhaust gas was varied up to +3%, the energy and exergy efficiencies of the system had the maximum variation of approximately 3%. And when T_{in} for the exhaust gas was varied up to ±2%, the energy and exergy efficiencies of the system had the maximum variation of approximately 5%. However, the net output of turbines and the propulsion efficiency, which are directly linked to the SFOC and SCE, were almost constant with the variation of the $C_{p,in}$ and T_{in} conditions. Although the conversion factor difference of ±10% for the mass flow rate of the exhaust gas directly influenced the output of the turbines and the propulsion efficiency including SFOC and SCE varied by about ±0.62%, the propulsion efficiency was slightly affected by the efficiency variations of ±5% for the pumps and turbines in the dual loop.

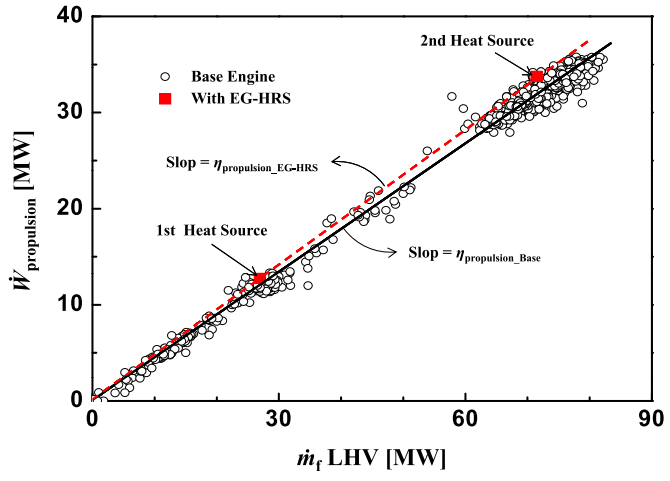

Fig. 12. Comparison of propulsive efficiency $\eta_{propulsion}$ for the base engine and the engine with the dual loop heat recovery system.

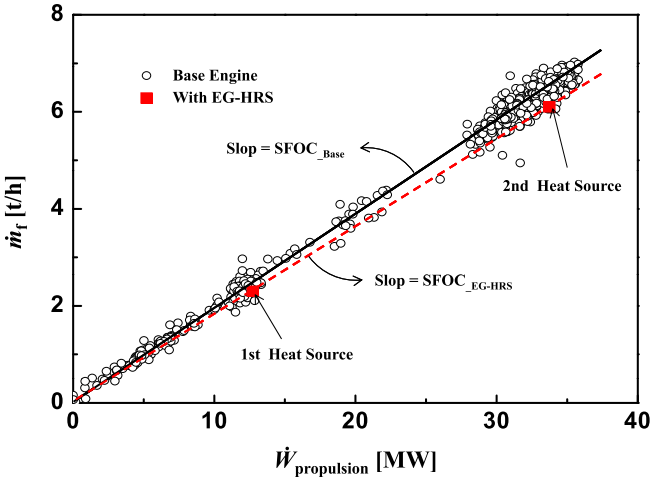

Fig. 13. Comparison of specific fuel oil consumption SFOC for the base engine and the engine with the dual loop heat recovery system.

Table 5
Error analysis for the difference of the thermodynamic assumptions in the dual loop heat recovery system.

At $T_1 = 327$ K	Ref. value	$C_{p,in}$	T_{in}	f_C	η_{p1}	η_{p2}	η_{t1}	η_{t2}
$C_{p,in}$ [kJ/kg K]	1.012	+3%	–	–	–	–	–	–
T_{in} [K]	510	–	±2%	–	–	–	–	–
f_C	53.8168	–	–	±10%	–	–	–	–
η_{p1}	0.85	–	–	–	±5%	–	–	–
η_{p2}	0.85	–	–	–	–	±5%	–	–
η_{t1}	0.85	–	–	–	–	–	±5%	–
η_{t2}	0.85	–	–	–	–	–	–	±5%
η_{sys}	0.1093	+2.84%	+4.67% −5.31%	0	−0.09% +0.09%	−1.01% +1.10%	−1.65% +1.56%	−4.39% +4.30%
$\eta_{sys,e}$	0.5877	+1.14%	+3.54% −2.99%	0	−0.03% +0.07%	−0.80% +0.90%	−1.11% +1.11%	−3.01% +3.03%
$\dot{W}_{net1}$ [kW]	719.8	0	0	−10.00% +9.99%	−0.24% +0.25%	0	−5.25% +5.24%	0
$\dot{W}_{net2}$ [kW]	1,350	0	0	−10.00% +10.00%	0	−1.56% +1.70%	+0.37% −0.37%	−6.67% +6.59%
$\eta_{propulsion}$	0.47236	0	0	−0.61% +0.61%	−0.01% +0.01%	−0.06% +0.07%	−0.10% +0.10%	−0.27% +0.26%
SFOC[g_{fue1}/kWh]	180.75	0	0	+0.61% −0.62%	+0.01% −0.02%	+0.06% −0.07%	+0.10% −0.10%	+0.27% −0.26%
SCE[g_{CO_2}/kWh]	545.5035	0	0	+0.61% −0.62%	+0.01% −0.02%	+0.06% −0.07%	+0.10% −0.10%	+0.27% −0.26%

Next, the long-term economic impact of the dual loop heat recovery system applied to the present container ship was discussed, with consideration of the repeating route. The SFS (Specific Fuel Saving) was defined as the total fuel quantity saved per route and is calculated as follows.

$$\text{SFS[kg/a route]} = \int \left(\Delta\text{SFOC} \times \dot{W}_{\text{shaft}}\right) dt \tag{37}$$

where ΔSFOC is the difference between the SFOC of the base engine and the SFOC of the engine using the exhaust gas heat recovery system. The above calculation indicated that a total fuel quantity of approximately 97.58 ton could be saved per route using the dual loop heat recovery system. Further, approximately 2341.89 ton of fuel can be saved per year when the route is regularly repeated as part of a round-trip twelve times a year.

5. Concluding remarks

A waste heat recovery power generation system for recovering exhaust gas heat discharged from a main engine and recycling it as a propulsion power was theoretically applied to a 6800 TEU container ship operating on a China–Korea–U.S. route. Two representative heat source conditions were selected based on actually measured data for the fuel consumption rate and exhaust gas temperature. In this case, a dual loop waste heat recovery power generation system with an upper trilateral cycle using water as the working fluid and a lower organic Rankine cycle using R1234yf as the working fluid was utilized, and the thermodynamic properties of the exhaust gas heat recovery system depending on changes in the boundary temperature between the upper cycle and the lower cycle, $T_1 = 320–375$ K, were studied.

The upper trilateral cycle showed that the amount of heat recovered from the evaporator and the amount of heat transmitted to the lower cycle from the upper cycle through a regenerator were reduced together, according to an increase in the boundary temperature. However, in the lower organic Rankine cycle, because the amount of heat transmitted to the preheater from the discharge gas heat source of the outlet of the evaporator was increased, loss was minimized with respect to the heat source of the exhaust gas ultimately discarded downstream of the preheater. Therefore, the net output of the dual loop waste heat recovery power generation system increased to $\dot{W}_{net} = 1,607.19–2,069.8$ kW, according to the increase in $T_1 = 320–375$ K.

At $T_1 = 375$ K, the dual loop heat recovery power generation system has a heat effectiveness of $\varepsilon = 0.8457$ and a cycle efficiency of $\eta_{cyc} = 0.1293$ (=12.93%), and as a result was confirmed to have a maximum system efficiency at $\eta_{sys} = 0.1093$ (= 10.93%). In such a case, the waste heat recovery system exhibited an exergy effectiveness of $\varepsilon_e = 0.9564$ and an exergy efficiency of $\eta_e = 0.6145$ (=61.45%), confirming maximum system exergy efficiency at $\eta_{sys,e} = 0.5877$ (=58.77%).

Consequently, the energy and exergy efficiencies of the dual loop system consisting of the upper trilateral cycle and lower organic Rankine cycle with a boundary temperature of $T_1 = 327$ K were improved in comparison with those of the single loop trilateral cycle with $T_1 = 305$ K. Further, the volumetric expansion ratio of the expander for the upper trilateral cycle in the dual loop heat recovery system could be significantly reduced with the increase in T_1 from 320 to 375 K.

When this dual loop heat recovery power generation system was applied to the main engine of the actual operating container ship, there was a propulsion efficiency of $\eta_{propulsion} = 0.47236$ (=47.236%), which theoretically confirms a 2.824% improvement in the propulsion power owing to the waste heat recovery system in comparison to the base engine, which has $\eta_{propulsion} = 0.44412$ (=44.412%). This improvement in the propulsion efficiency was confirmed to lead to the reduction in the specific fuel oil consumption of the main engine during actual operation from SFOC = 192.41 to 180.75 $g_{\_fuel}$/kWh, and reduction in the Specific CO_2 Emission by about 6.06% from SCE = 580.6934 to 545.5035 $g_{\_CO_2}$/kWh.

Acknowledgments

This work was supported by the Korea Institute of Marine Science & Technology under Grand Number 1615006035-201101532.

References

[1] Buhaug Ø, Corbett JJ, Endresen Ø, Eyring V, Faber J, Hanayama S, et al. Second IMO GHG study 2009. London, UK: International Maritime Organization (IMO); 2009.
[2] Amendments to MARPOL annex VI on regulations for the prevention of air pollution form ships by inclusion of new regulations on energy efficiency for ships. London, UK: International Maritime Organization (IMO); 2011. MEPC 62/24/Add.1.
[3] Draft guidelines on the method of calculation of the attained energy efficiency design index for new ships. London, UK: International Maritime Organization (IMO); 2011. MEPC 62/5/4.
[4] MAN Diesel & Turbo. Thermo efficiency system for reduction of fuel consumption and CO_2 emission. Copenhagen, Denmark 2005.
[5] MAN Diesel & Turbo. Waste heat recovery system (WHRS) for reduction of fuel consumption, emissions and EEDI. Copenhagen, Denmark 2012.
[6] Wang EH, Zhang HG, Fan BY, Ouyang MG, Zhao Y, Mu QH. Study of working fluid selection of organic Rankine cycle (ORC) for engine waste heat recovery. Energy 2011;36:3406–18.
[7] Bombarda P, Invernizzi CM, Pietra C. Heat recovery from diesel engines: a thermodynamic comparison between Kalina and ORC cycles. Applied Thermal Engineering 2010;30:212–9.

[8] He M, Zhang X, Zeng K, Gao K. A combined thermodynamic cycle used for waste heat recovery of internal combustion engine. Energy 2011;36:6821–9.
[9] Vaja I, Gambarotta A. Internal combustion engine bottoming with organic rankine cycles. Energy 2010;35:1084–93.
[10] Teng H, Regner G, Cowland C. Achieving high engine efficiency for heavy-duty diesel engines by waste heat recovery using supercritical organic-fluid Rankine cycle. SAE Paper No. 2006-01-3522.
[11] Teng H, Regner G. Improving fuel economy for HD diesel Engines with WHR Rankine cycle driven by EGR cooler heat rejection. SAE Paper No. 2009-01-2913.
[12] Wang EH, Zhang HG, Zhao Y, Fan BY, Wu YT, Mu QH. Performance analysis of a novel system combining a dual loop organic Rankine cycle (ORC) with a gasoline engine. Energy 2012;43:385–95.
[13] Zhang HG, Wang EH, Fan BY. A performance analysis of a novel system of a dual loop bottoming organic Rankine cycle (ORC) with a light-duty diesel engine. Applied Energy 2013;102:1504–13.
[14] Fischer J. Comparison of trilateral cycles and organic rankine cycles. Energy 2011;36:6208–19.
[15] Technical file for HYUNDAI-MAN B&W 12K98MC-C Mk6. Ulsan, Korea: Hyundai Heavy Industries Co., Ltd.; 2006.
[16] Tupper EC. Introduction to naval architecture. 4th ed. Oxford, UK: Elsevier Butterworth-Heinemann; 2004.
[17] Shintani K, Imai A, Nishimura E, Papadimitriou S. The container shipping network design problem with empty container repositioning. Transportation Research Part E 2007;43:39–59.
[18] Boyce MP. Handbook for cogeneration and combined cycle power plants. 2nd ed. New York, USA: ASME Press; 2010.
[19] Amendment to the technical code on control of emission of nitrogen oxides from marine diesel engines (NOx technical code 2008). London, UK: International Maritime Organization (IMO); 2008. MEPC 58/23/Add. 1.
[20] Prevention of air pollution from ships-updated 2000 study on greenhouse gas emissions from ships phase 1 report. London, UK: International Maritime Organization (IMO); 2008. MEPC 58/INF. 6.
[21] Law CK. Combustion physics. New York, USA: Cambridge University Press; 2006.
[22] Cengel YA, Boles MA. Thermodynamics: an engineering approach. 5th ed. Singapore: McGraw-Hill; 2006.
[23] Moran MJ, Shapiro HN. Fundamentals of engineering thermodynamics. 6th ed. Chichester, England: John Wiley & Sons; 2006.
[24] Kaminski DA, Jensen MK. Introduction to thermal and fluids engineering. New Jersey, USA: John Wiley & Sons Inc; 2005.
[25] Dipippo R. Ideal thermal efficiency for geothermal binary plants. Geothermics 2007;36:276–85.
[26] Yamada N, Mohamad MNA, Kien TT. Study on thermal efficiency of low- to medium-temperature organic Rankine cycles using hfo-1234yf. Renewable Energy 2012;41:368–75.
[27] Calm JM. The next generation of refrigerants-historical review, considerations, and outlook. International Journal of Refrigeration 2008;31:1123–33.
[28] Honeywell. HFC-134a material safety data sheet 2005.
[29] Honeywell. HFO-1234yf material safety data sheet 2008.
[30] Liu BT, Chien KH, Wang CC. Effect of working fluids on organic Rankine cycle for waste heat recovery. Energy 2004;29:1207–17.
[31] Shipbuilding-sea water temperature for designing marine heat exchangers. Japanese Standards Association; 2006. JIS F 0502-2006.
[32] Smith IK. Development of the trilateral flash cycle system part 1: fundamental considerations. Proceedings of Institution of Mechanical Engineers, Part A 1993;207:179–94.
[33] Klein SA. Engineering equation solver (EES) Prof. Ver. 8.830.
[34] Smith IK, Stosic N, Aldis CA. Development of the trilateral flash cycle system Part 3: the design of high efficiency two-phase screw expanders. Proceedings of Institution of Mechanical Engineers, Part A 1996;210:75–93.
[35] Dietlen S, Hieronymus H, Plewinsky B, Schröder V, Steen H. Explosion behavior of the 'non-flammable' CFC substitute 1,1,1,2-tetrafluoroethane (R134a). Chemical Engineering and Processing 1995;34:141–9.
[36] Kondo S, Takizawa K, Tokuhashi K. Effects of temperature and humidity on the flammability limits of several 2L refrigerants. Journal of Fluorine Chemistry 2012;144:130–6.
[37] Emergency response guidelines for anhydrous hydrogen fluoride (HF). Virginia, USA: American Chemistry Council; 2007.
[38] Soot deposits and fires in exhaust gas boilers. Copenhagen, Denmark: MAN Diesel & Turbo SE; 2004.
[39] Chen H, Goswami Y, Stefankos EK. A review of thermodynamic cycles and working fluids for the conversion of low-grade heat. Renewable and Sustainable Energy Reviews 2010;14:3059–67.
[40] Heywood JB. Internal combustion engine fundamentals. New York, USA: McGraw-Hill Int; 1988.